

# Resonant carrier dynamics in biased superlattices in presence of dissipation

Pavel Abumov and D. W. L. Sprung

*Department of Physics and Astronomy, McMaster University  
Hamilton, Ontario L8S 4M1 Canada*

(Dated: April 3, 2019)

We study electron dynamics in a biased undriven ideal semiconductor superlattice near energy level anticrossings, in the presence of dissipation due to homogeneous level broadening. In particular, we examine the dependence of wavepacket dynamical characteristics on electric field detuning, and investigate mixed regimes involving a superposition of energy level anticrossings with both Rabi oscillations and resonant Zener tunneling. In present work, Rabi and Zener resonances were shown to have same origin and a criterion for the occurrence of either was proposed. The results obtained allow a better understanding of the nature of an interminiband resonance, and can be used in the areas of microwave radiation generation and matter manipulation on the particle level.

PACS numbers: 73.23.-b, 73.21.Cd, 78.20.Bh, 78.30.Fs

## I. INTRODUCTION

Carrier dynamics in a biased superlattice (SL) has remained an active topic during the last two decades. Knowledge of the underlying physical processes is necessary for a better understanding of perpendicular transport of carriers in multi-quantum well systems, as well as for successful development of potential applications, such as microwave radiation generation [1, 2, 3, 4], quantum computing [5, 6] and matter manipulation on particle level [7].

Studies focused on coherent carrier dynamics revealed some dynamical features of great interest (see, for example, [8] and [9] and references therein). However, even more important aspects of resonant dynamics in a SL comes from the interplay between coherent interminiband oscillations and incoherent tunneling to the continuum. This question goes back to the famous quantum-mechanical problem of tunneling in presence of dissipation [10, 11, 12] and has been considered for superlattice by few authors [13]. Whereas typically a solution involves a number of approximations and constraints, we chose a computational approach with few limitations. This enabled us to consider resonant dynamics at high and moderate bias, specifically Rabi oscillations (RO) and resonant Zener tunneling (RZT), and to establish a relation between these two fundamental types of interminiband transport. In the first place, it helps in understanding the damping mechanism of RO and to propose ways to reduce it. It also allows to make a link between RO and RZT, an instance where quantum transport theory has been lacking to date. The results obtained can be applied to any systems possessing Wannier-Stark ladder structure, e.g. some photonic crystals [14].

## II. RESONANT INTERMINIBAND DYNAMICS

This work is focussed on longitudinal motion of a single electron in a zero-temperature biased superlattice. The model is described by the time-dependent Schrödinger

equation

$$-\frac{\hbar^2}{2mm^*}\nabla^2\Psi(x,t) + (V_{SL}(x) + xF)\Psi(x,t) = E\Psi(x,t)$$

with  $V_{SL}(x) = \frac{V_0}{2} \left[ \tanh \frac{x+a/2}{\sigma} - \tanh \frac{x-a/2}{\sigma} \right]$  (1)

where  $\Psi(x,t)$  is an electron wavefunction,  $F = -eE$  is a uniform bias, and  $V_{SL}(x)$  is a model potential representing a unit cell of the periodic system. Parameters of the several GaAs/Ga<sub>1-x</sub>Al<sub>x</sub>As layered heterostructures considered are shown in Table I. The numerical solution of Eq. 1 used discrete transparent boundary conditions [9, 15].

The norm of the quasibound part of the wavepacket  $\rho$  and miniband occupancy  $\rho_\nu$  provide a convenient means to monitor interminiband dynamics; miniband occupancy means the wavepacket projection on a tight-binding miniband  $\nu$ :  $\rho_\nu = \sum_k |\langle \Psi(x,t) | W_\nu^k(x) \rangle|^2$ . Here  $W_\nu^k(x)$  stands for a Wannier-Stark (WS) quasibound state corresponding to energy level  $E_\nu^k$  centered on the well with index  $k$ , and belonging to miniband  $\nu$  ( $\nu=1,2,\dots$ ); the initial wavepacket is centered on the well with index 0. The tight-binding Wannier functions from miniband  $\nu$  are denoted as  $w_\nu(x)$ .

To refer to an interminiband resonance originating from an anticrossing of energy levels  $E_\nu^k$  and  $E_\mu^{k+n}$  in biased sample X, we will use the symbol  $\mathcal{R}_{\nu\mu}^n(\mathbf{X})$  and we will denote the resonant bias (the value of bias at which the peak of a resonance is observed) as  $F_n$ ,  $n$  being the resonance index ( $n = 1, 2, \dots$ ). When of little importance, some indices may be omitted for brevity. Symbol  $G$  will stand for inverse bias  $1/F$  ( $G_n$  corresponds to  $1/F_n$ ). Unless specified otherwise, time is expressed in units of the Bloch period  $T_B = 2\pi\hbar/Fd$ .

### A. Rabi oscillations model

Typically, Rabi oscillations are a result of interminiband transitions under external radiation when its frequency approaches the inherent system's value  $\omega_{12} =$

arXiv:0712.0436v1 [cond-mat.mtrl-sci] 4 Dec 2007

Name	$V_0$ , meV	$d$ , nm(ML)	$a$ , nm(ML)	$\sigma$ , nm
Sample A	212	13.0 (46)	3.1 (11)	0.4
Sample B	250	17.3 (61)	2.5 (9)	0.4
Sample C	212	13.0 (46)	2.3 (8)	0.4
Sample D	212	13.0 (46)	2.5 (9)	0.4

TABLE I: Geometric parameters of the model potentials used in simulations. Barrier height of 212 meV corresponds to  $x=0.18$  and of 250 meV to  $x=0.3$  in the GaAs/Ga<sub>1-x</sub>Al<sub>x</sub>As structure; ML stands for monolayer thickness, 1 ML = 0.283 nm.

$(E_2 - E_1)/\hbar$  [16]. This pumping provides excitation of carriers with their subsequent spontaneous emission, which is widely used in quantum cascade lasers [17]. A comprehensive overview of RO in the two-miniband approximation has been given by Ferreira and Bastard [18] and more mathematical details can be found in references [19, 20, 21]. In a biased SL, interminiband transitions may also happen in the absence of external radiation [22, 23, 24]: once energy levels from coupled WSL align in neighboring wells, a carrier can easily tunnel between them while undergoing non-radiative transitions.

For an undriven SL (i.e. not exposed to an external oscillating electric field) a fruitful analogy can be made to the well-described system of a two-level atom under external monochromatic radiation  $V(t) = E_0\mu \cos(\omega t)$ , where  $\hat{\mu} = \hat{x}$  is the dipole transition operator between MB1 and MB2, and  $E_0$  is the amplitude of the external electric field. Let us take the WS states to be stationary and orthogonal, assuming very large carrier lifetime  $1/\Gamma$  compared to a typical RO period for a moderate bias. With that, the acceleration theorem  $\hbar \frac{d\vec{k}}{dt} = \vec{F}$ , combined with the dispersion relation can describe wavepacket evolution over a Bloch oscillation cycle, by using the decomposition  $V(x) = V_{SL} + Fx$ :

$$\langle x(t) \rangle = \frac{1}{\hbar} \int_0^t \frac{dE(k_0 + Ft/\hbar)}{dk} dt \quad (2)$$

In the case of tightly bound lowest minibands, common for a semiconductor SL, carrier dispersion in MB $n$  can be approximated as  $E(k) = E_n + (\delta E/2) \cos(kd + n\pi)$  and the mean position evolves as  $\langle x(t) \rangle = (L/2)(\cos(\omega_B t) - 1)$  for  $F > 0$ , where  $\omega_B$  is the Bloch angular frequency and  $L$  is the Bloch oscillation domain width. If the real-space origin is placed at  $\langle x(t) \rangle$ , the wavepacket's evolution in space with its energy being conserved can heuristically be replaced by its evolution in kinetic energy space, while retaining a fixed mean real-space position. The effective potential in MB $n$  then becomes  $V_n(x, t) = V_{SL}(x) + \frac{\delta E_n}{2} \cos(\omega_B t + n\pi)$  that looks much like potential of an irradiated atom: the system has a natural frequency  $\omega_{12} = (E_2 - E_1)/\hbar$  and is effectively driven by Bloch frequency. The Hamiltonian for such

system at resonance field  $F_n$  becomes

$$i\hbar \frac{\partial \Psi(x, t)}{\partial t} = (\hat{H}_0 + \hat{V}) \Psi(x, t) \quad (3)$$

with  $\hat{V} = \hat{x} F_n \cos(\omega_B t)$ ,

where  $\hat{H}_0$  refers to an undriven biased SL in the tight-binding approximation. An expression for the population of the second level with initial wavepacket  $\Psi(x, 0) = W_1(x)$  can be now obtained in the same fashion as for an atom-like system [16]. Simple calculations show that in our case

$$\omega_{12} - \omega \equiv \omega_{12} - n\omega_B = \frac{(E_1 - E_2)^2}{nd\hbar} (G_n - G)$$

is the difference between the system's frequency at the  $n^{\text{th}}$  resonance, and the driving BO frequency. With necessary modifications, for a two-level system driven off its ground state we obtain

$$\frac{\rho_2}{\rho}(t) = \left(\frac{\rho_2}{\rho}\right)^{max} \mathcal{L}(G) \sin^2 \frac{\pi t}{T_R^{max} \sqrt{\mathcal{L}(G)}}$$

$$\frac{\rho_1}{\rho}(t) = 1 - \frac{\rho_2}{\rho}(t), \quad (4)$$

where

$$\mathcal{L}(G) \equiv \left( \left( \frac{G - G_n}{\Gamma} \right)^2 + 1 \right)^{-1} \quad (5)$$

$$\Gamma = \frac{x_{0n}}{E_2 - E_1}$$

$$T_R^{max} = \frac{d}{x_{0n}}$$

$$x_{nm} = \langle W_1^n(x) | x | W_2^m(x) \rangle, \quad (6)$$

with  $d$  being the SL period. These equations are straightforward to generalize for an arbitrary couple of interacting minibands. Note that in order to predict the  $\rho_2/\rho(t)$  curve in the entire near-resonant region we require only values of the dipole matrix element  $x_{nm}$  and of  $(\rho_2/\rho)^{max}$  computed at a the resonant bias field. In this simplistic

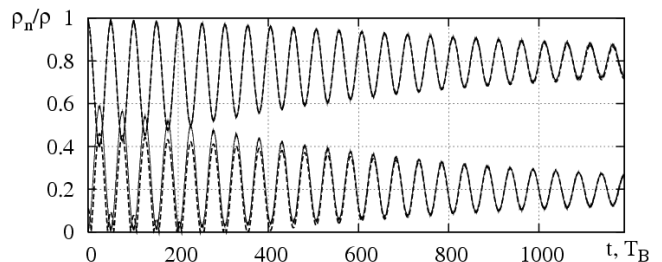


FIG. 1: Occupancy functions (solid lines) and their fit from Eq. 7 (broken line) for  $\Psi(x, 0) = w_1(x)$  near resonance  $\mathcal{R}_{12}^3(\mathbf{A})$  at  $G = 0.44058$  nm/meV (0.8 HWHM away from the resonant bias); the upper curve corresponds to  $n = 1$  and the lower to  $n = 2$ .

derivation for a two-level tightly bound system, we have neglected dispersion of the wavepacket in the process of BO, nonetheless it can give a quite satisfactory explanation as will be seen below.

We will consider moderate fields, where the BO domain is typically smaller than a potential cell width; that implies that: (i) Energy levels are sparse due to large splitting of WSL; hence near a resonance there is one preferred tunneling path between MB1 and MB2; (ii) At a resonance, WS states are reasonably localized and have an exponentially vanishing tail, so we expect that  $x_{0n} \propto e^{-n}$  (this has been predicted by a two-level model for an atom [23] and also has been explicitly calculated for a multiband driven SL [25]).

The above derivations were made for system in a steady state. However, in practice an initial non-equilibrium configuration undergoes a relaxation process. To study this we used a linear combination  $\Psi(x) = c_1 w_1(x) + c_2 w_2(x)$  as the initial wavefunction  $\Psi(x, 0)$  in Eq. 1. Obtaining correct quasibound WS functions is a significant task in itself [25, 26] and is not important for our primary goal to study steady-state RO dynamics. The mechanisms underlying the steady tunneling process do not depend on the particular linear combination: the higher miniband components of  $\Psi(x)$  tunnel out at a high rate during the initial relaxation period, which only scales down the norm of the quasibound wavepacket being observed in a steady mode. The coefficients  $c_1$  and  $c_2$  were set so that upon the initial period of relaxation of a non-equilibrium state the resulting RO were clear and of sufficient magnitude; the maximum of RO magnitude reaches nearly unity for the two extreme cases  $|c_1| = 1$  and  $|c_2| = 1$ , with less carrier decay for the former. Hence, for the convenience we chose the initial wavefunction in the form  $\Psi(x) = w_1(x)$  without loss of generality.

## B. Near-resonance parameter behavior

By studying isolated Rabi resonances, it has been found that a carrier undergoing RO produces damped oscillations in miniband occupancy of the form:

$$\rho_n(t) = \rho(t) \left( P_n + A_R e^{-\gamma_A t} \cos\left(\frac{2\pi t}{T_R} + \phi_n\right) \right)$$

$$\text{with } \rho(t) = \exp\left(-\gamma t - \sigma(1 - e^{-\gamma_{nc} t})\right) \quad (7)$$

in agreement with the general theory [27]. Here  $T_R$ ,  $A_R$  and  $\gamma_A$  are the period, amplitude and decay rate of Rabi oscillations respectively;  $\phi_n$  is an initial phase determined by a particular form of  $\Psi(x, 0)$  (e.g.  $\phi_1 \approx 0$  for  $\Psi(x) = w_1(x)$ );  $\gamma$  is the decay rate of the entire wavepacket and  $P_n$  is asymptotic value of  $\frac{\rho_n}{\rho}(t)$  in the limit of  $t \rightarrow \infty$ . The term  $-\sigma(1 - e^{-\gamma_{nc} t})$  represents a dip in the decay rate due to two-exponential decay [28] and was found to be vanishingly small close to the resonant bias. Its presence is due to the initial relaxation

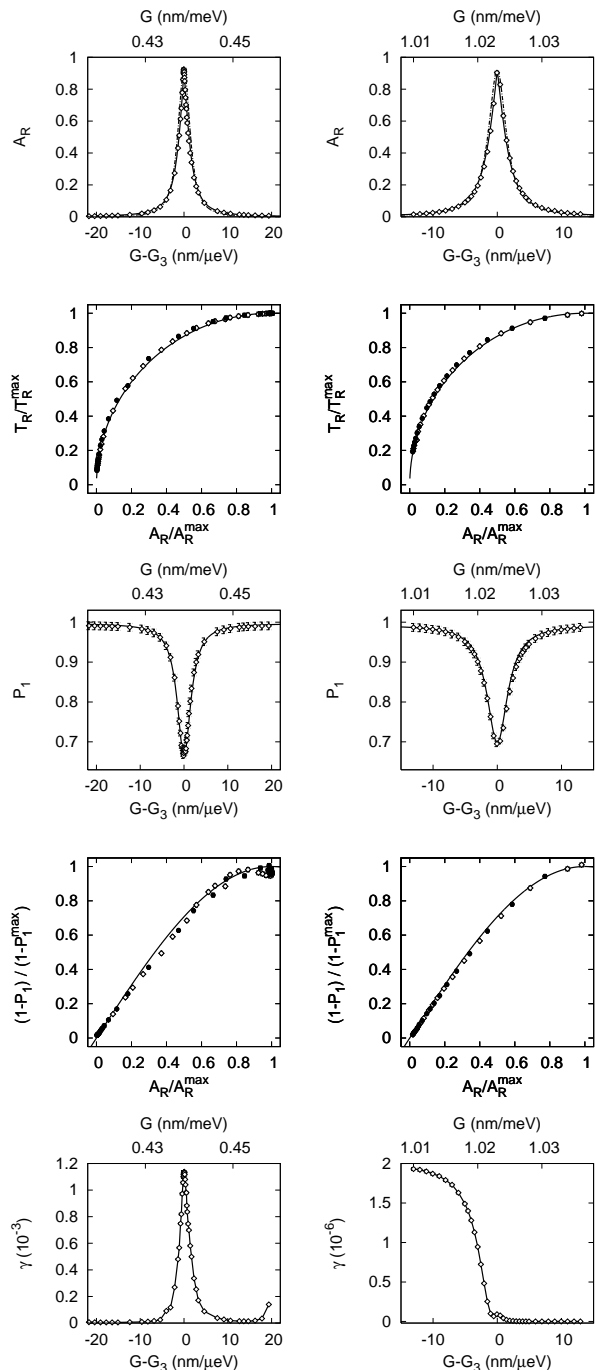


FIG. 2: Behavior of key dynamical parameters for  $\mathcal{R}_{12}^3(\mathbf{A})$  (left) and  $\mathcal{R}_{12}^3(\mathbf{B})$  (right). Top panel shows displays RO amplitude vs. inverse bias (chain-dotted line shows a Lorentzian fit  $\mathcal{L}_{12}^3(G)$ , solid line shows fit from Eq. 10), second from top panel: relative RO amplitude vs. relative RO period (filled circles correspond to  $G < G_3$ , empty circles to  $G > G_3$ ; solid line shows fit from Eq. 10 given Eq. 9), third from top panel: asymptotic occupancy of the first miniband vs. inverse bias (solid line shows fit from Eq. 10 given Eq. 10), fourth from top panel: relative RO period vs. asymptotic occupancy of the first miniband (filled circles correspond to  $G < G_3$ , empty circles to  $G > G_3$ ; solid line shows fit from Eq. 10), bottom panel: carrier decay rate vs. inverse bias.

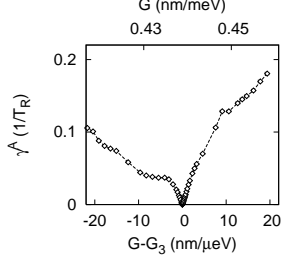


FIG. 3: Damping rate of RO vs. inverse bias for  $\mathcal{R}_{1-2}^3(\mathbf{A})$  in  $1/T_R$  units.

of the wavepacket part orthogonal to eigenfunctions of the current miniband, with  $\sigma$  being proportional to the norm of the orthogonal part and  $\gamma_{ne}$  being the relaxation rate, typically larger by two orders of magnitude than  $\gamma$ . A typical example of near-resonant interminiband occupancy dynamics and its fit from Eq. 7 is demonstrated in Fig. 1.

Since the set of parameters in Eq. 7 provides a good description of carrier dynamics, we focus on examining their behavior around a resonance. As was shown previously [9], the period of Rabi oscillations shows a Lorentzian-like peak around the resonant bias:

$$T_R = T_R^{max} \sqrt{\mathcal{L}_{\nu\mu}^n(G)} \quad (8)$$

$$\mathcal{L}_{\nu\mu}^n(G) = \left[ \left( \frac{G - G_n}{\Gamma} \right)^2 + 1 \right]^{-1}$$

Further we will refer to Lorentzian parameter  $\Gamma$  as the HWHM of the resonance under consideration.

For a double quantum well system, the perturbation theory predicts that the frequency of Rabi oscillations strictly at resonant bias equals  $\omega_R = \frac{2}{\hbar} \langle \Psi_L | V(x) | \Psi_R \rangle$ . Here  $\langle \Psi_L | V(x) | \Psi_R \rangle$  is the tunneling matrix element through the barrier separating the two wells [27] and is essentially the splitting between the energy levels. Thus  $T_R^{max}$  from Eq. 9 has the meaning of being an inverse measure of the minimum energy level splitting at their anticrossing.

As derived from the simulation results, the parameters  $A_R$  and  $P_n$  have clear extrema as well. The following equations fit the data quite well (Fig. 2):

$$A_R = A_R^{max} \left[ 1 - \sqrt{1 - \mathcal{L}_{\nu\mu}^n(G)} \right], \quad (9)$$

$$\tilde{P}_n = \tilde{P}_n^{max} \sin \left( \frac{\pi A_R}{2 A_R^{max}} \right), \quad (10)$$

with  $A_R^{max}$  and  $\tilde{P}_n^{max}$  being the peak values;  $\tilde{P}_n = P_n$  for the lower resonantly coupled MB and  $1 - P_n$  for the upper one. The other two parameters,  $\gamma$  and  $\gamma_A$ , are extremely sensitive to coupling to higher minibands and their bias

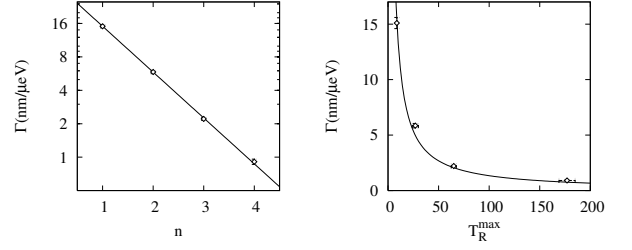


FIG. 4: Logarithmic fit of  $\Gamma_n$  versus resonance index for  $\mathcal{R}_{1-2}(\mathbf{A})$  (left) and its relation to  $T_R^{max}$  (right).

detuning dependence varies from one resonance to another. However, at a resonant bias  $\gamma_A$  always reached its virtually zero minimum, and  $\gamma$  its maximum (Fig. 2, 3).

As the index  $n$  rises,  $\mathcal{R}_{\mu-\nu}^n$  are expected to become narrower, since the length of the tunneling pathway into the adjacent miniband increases and so does the system's sensitivity to bias detuning, due to related frequency detuning of the Bloch oscillations; this is reflected in a decrease of  $x_{0n}$  in Eq. 6. We have shown previously [9] that the peak period of Rabi oscillations changes exponentially with resonance index  $n$ :

$$T_n^{max} = T_1^{max} \left( T_2^{max} / T_1^{max} \right)^{n-1}.$$

As predicted by Eq. 6, the resonance HWHM dependence on  $n$  closely follows an exponential law (Fig. 4) as well:

$$\Gamma_n = \Gamma_1 \left( \Gamma_2 / \Gamma_1 \right)^{n-1} \quad (11)$$

The anticipated 6 relation

$$T_n^{max} = G_0 (\Gamma_n)^{-1} \quad (12)$$

also holds quite well: fitting equation 11 produced a value  $T_n^{max} \Gamma_n = (139 \pm 5)$  nm/ $\mu$ eV compared to  $G_0 = (145 \pm 1)$  nm/ $\mu$ eV for sample A, and calculations for sample B showed that  $T_3^{max} \Gamma_3 = (1.05 \pm 0.01)$  nm/meV compared to  $G_0 = (1.02 \pm 0.01)$  nm/meV.

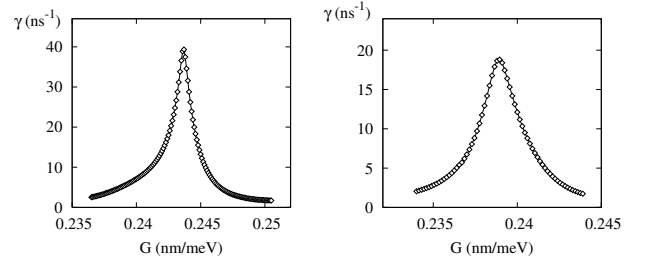


FIG. 5: Decay rate  $\gamma$  of a wavepacket vs. inverse bias, near  $\mathcal{R}_{23}^5(\mathbf{C})$  (left) and  $\mathcal{R}_{23}^6(\mathbf{D})$  (right).

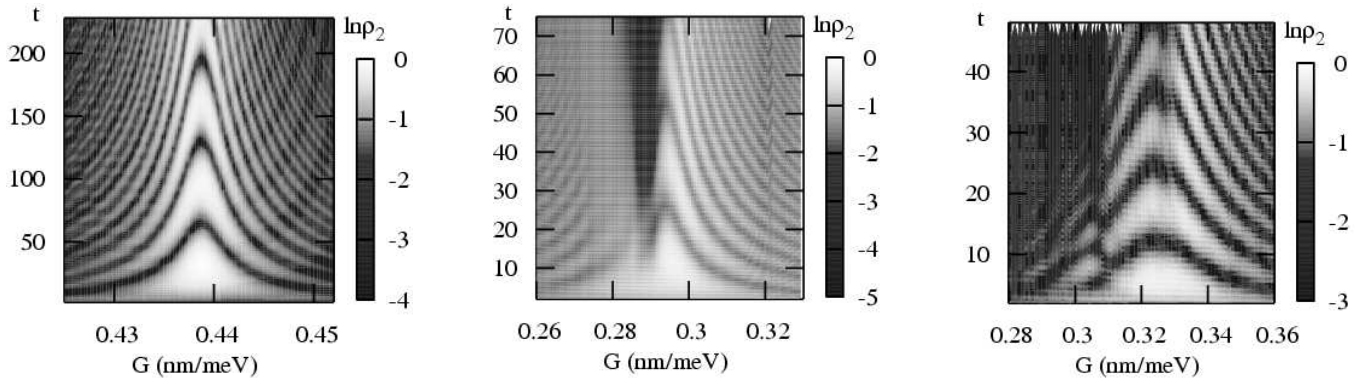


FIG. 6: Near-resonant dynamics of second miniband occupancy at  $\mathcal{R}_{12}^3$ (A) (left),  $\mathcal{R}_{12}^3$ (C) (center) and  $\mathcal{R}_{12}^2$ (B) (right).

When an ensemble of resonantly coupled minibands is weakly bound, resonant Zener tunneling (RZT) [29, 30, 31] prevails over RO; we will call these Zener resonances. In this case the carrier excitation decays very quickly and does not exhibit persistent RO. Then  $\gamma$  becomes the key parameter in the dynamical description and features a clear peak centered about the resonant bias (Fig. 5). Sensitivity of  $\gamma$  to coupling to higher minibands makes the shape of curves  $\gamma(G)$  differ for different resonances.

### III. RABI OSCILLATIONS AND RESONANT ZENER TUNNELING

In section IIB we have been considering isolated interminiband resonances; typically, they occur in a strong potential at moderate fields where resonances have small HWHM compared to their spacing in inverse bias space and hence they rarely overlap. In a more realistic example of a high-field resonance in a weaker potential, the interaction between just two resonantly coupled minibands represents only one of many interference paths. For mod-

erate potentials, such as  $\text{Al}_{0.3}\text{Ga}_{0.7}\text{As}$ , incoherent coupling to higher minibands has strong enough influence on overall dynamics and one can observe mixed regimes exhibiting overlapping Zener and Rabi resonances that cause simultaneous resonant Zener tunneling and Rabi oscillations.

#### A. Superposition of resonances

We now consider a case of overlapping Rabi and Zener resonances, to illustrate how coherent and incoherent dynamics interfere at a near-resonant bias. This typically occurs when the HWHM of a Rabi resonance is large compared to the HWHM of a Zener resonance, since the latter requires coupling to the higher minibands. Then one resonance is seen to be superimposed on another, as in the center panel of Fig. 6. At the  $\mathcal{R}_{13}^5$  peak, RO vanish and the  $P_1(G)$  and  $A_R(G)$  curves demonstrate a sharp extremum indeed resembling a superposition of two Lorentzian-like curves (Fig. 7).

The close presence of a Zener resonance shifts the

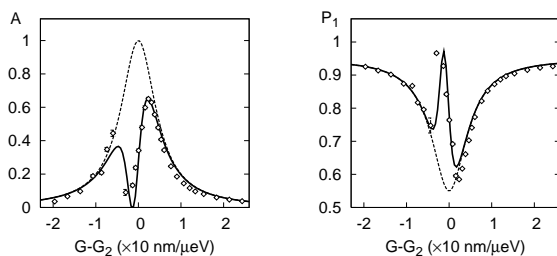


FIG. 7: Amplitude of RO and of first miniband occupancy near resonances  $\mathcal{R}_{12}^2$  and  $\mathcal{R}_{13}^5$  from Fig. 6. Solid lines show a superposition of Lorentzian curves best fitting simulation data, in circles; broken line is a projection of a fit in the absence of  $\mathcal{R}_{13}^5$ .

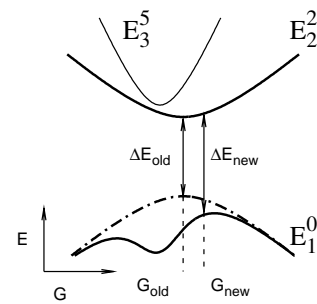


FIG. 8: Schematics showing mutual impact of energy levels anticrossings. Chain-dotted line shows position of level  $E_1^0$  in the absence of repulsion from level  $E_3^5$ , shown in thin solid line.

Rabi resonance peak along the bias scale. From the relation  $F_n = F_0 n$ , the resonance  $\mathcal{R}_{12}^2$  (from center panel of Fig. 6) would have a peak at  $G = (0.284 \pm 0.002)$  nm/meV; however as the maximum period of oscillations indicates, it is located at a lower bias  $G = (0.295 \pm 0.002)$  nm/meV. At the energy level anticrossing corresponding to  $\mathcal{R}_{13}^5$  the levels  $E_0^1$  and  $E_3^5$  are repelled from each other [25] while having little effect on  $E_2^2$ . The minimum of the mismatch  $E_2^2 - E_0^1$  produces the longest period of RO [9]. Hence, the peak of a Rabi resonance, may shift as demonstrated in Fig. 8. There the energy difference minimum at  $\mathcal{R}_{12}^2$   $\Delta E_{old}$  located at  $G_{old}$  in the absence of  $\mathcal{R}_{13}^5$  anticrossing shifts to  $G_{new}$  due to superposition of the energy level anticrossings  $\mathcal{R}_{12}^2$  and  $\mathcal{R}_{13}^5$ . Since the repulsion from the two anticrossings adds up,  $\Delta E_{old}$  is larger than  $\Delta E_{new}$ , and since the RO period is inversely proportional to the mismatch in energy level alignment, the peak period of RO shifts to a new value of bias. Thus the proximity of another resonance has a twofold effect on the resonance considered: it shifts its resonant bias and reduces the maximum period of RO. The latter effect is demonstrated in the right panel of Fig. 6, where a weak and narrow Zener resonance spread over  $G = 0.322 \dots 0.330$  nm/meV reduces the RO period.

### B. Conditions for Rabi resonance

The issue of RO persistence leads in the direction of separating coherent from incoherent dynamics. The simulation data reveal that a slower decay of RO occurs far from Zener resonances and in stronger potentials, with strongly bound lowest minibands reducing the carrier decay rate  $\gamma$ . At the same time, the RO decay rate nearly vanishes at the very peak of a Rabi resonance where the wavepacket tunneling rate is at its highest. Thus the tunneling rate by itself is not a reliable indicator of Rabi oscillation damping. Fig. 9 demonstrates Zener tunneling and Rabi oscillation patterns at the same tunneling

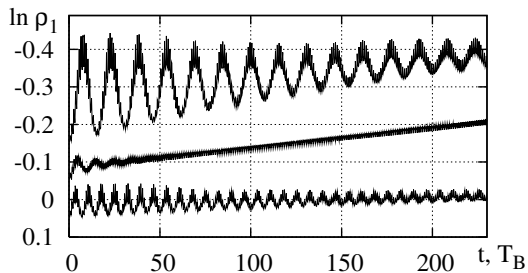


FIG. 9: Dynamics of first miniband occupancy in the vicinity of  $\mathcal{R}_{12}^2$ , from the center panel of Fig. 6 at  $G_1 = 0.274$  nm/meV (lower curve),  $G_2 = 0.274$  nm/meV (middle curve) and  $G_3 = 0.301$  nm/meV (upper curve). The upper [lower] curve is shifted upwards [downwards] by 0.1 for visibility.

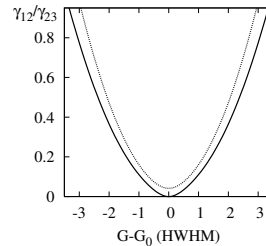


FIG. 10: Ratio of interminiband tunneling rates  $\gamma_{12}/\gamma_{23}$  vs. inverse bias (in resonance HWHM units), from Eq. 14 given Eq. 10. Solid and broken lines show the cases when  $P_1 = 0.5$  and  $0.6$  at resonance, correspondingly.

rate, observed for bias values  $F_2$  and  $F_3$ , respectively. In the center panel of Fig. 6 at  $G_1 = 0.312$  nm/meV there is a clear RO pattern, whereas at the bias  $G_2 = 0.274$  nm/meV which is symmetric to  $G_1$  about the Rabi peak (located at  $G_0 = 0.293$  nm/meV), Rabi oscillations die out quickly. This behavior does not agree with the previously found symmetric structure of an isolated resonance (left panel of Fig. 6); it is interference of a Zener resonance at  $G_2$  that overdamps the Rabi oscillations. To generalize, the alignment of energy levels from higher minibands sets the wavepacket behavior model and the link between RO and RZT (that are both a product of wavepacket self-interference) is determined by a particular arrangement of WS ladders: specifically, by the ratio of interminiband tunneling rates as will be shown below.

For illustrative purposes, let us again turn to the two-miniband model and denote the rate of tunneling from  $MB\nu$  to  $MB\mu$  as  $\gamma_{\nu\mu}$ ; this is a convenient measure of strength of interminiband coupling. The magnitude of  $\gamma_{\nu\mu}$  is inversely proportional to the difference in energy between the resonantly coupled energy levels from  $WSL\nu$  and  $WSL\mu$  [32]. In case of Fig. 9, these level pairs are:  $E_1^0$  and  $E_2^2$  for the Rabi resonance and  $E_1^0$  and  $E_3^5$  for the Zener resonance. For the inverse biases  $G_2$  and  $G_3$  featuring the same carrier decay rate (from the example above), the difference  $(E_2^2 - E_1^0) - \Delta E_{21}$  determining the tunneling between  $MB1$  and  $MB2$  is  $-2$  meV and  $6.2$  meV, correspondingly ( $\Delta E_{21}$  is the energy spacing between the centers of  $MB2$  and  $MB1$  which equals  $88.8$  meV for potential A), whereas at the same values of bias,  $(E_3^5 - E_1^0) - \Delta E_{31}$  for the ensemble of  $MB1$  and  $MB3$  equals  $-10$  meV and  $10$  meV. Considering that the width of tight-binding  $MB1$ ,  $MB2$  and  $MB3$  is  $8.8$ ,  $39.4$  and  $98.6$  meV, the disparity between the two values of  $(E_2^2 - E_1^0) - \Delta E_{21} \propto 1/\gamma_{12}$  is much more significant than that of  $(E_3^5 - E_1^0) - \Delta E_{31} \propto 1/\gamma_{13}$ . Hence, the ratio  $\gamma_{12}/\gamma_{23}$ , which shows the strength of isolation of the coupled ensemble of  $MB1$  and  $MB2$  from higher minibands, is much smaller in the case of  $G_2$ . Due to a weaker isolation of the ensemble at  $G_2$ , the quasibound oscillating part of the wavepacket is more subject to incoherent tun-

neling into the continuum, so RO are destroyed and turn more quickly into RZT.

This also explains why at the peak of an isolated Rabi resonance, RO damping rate is the lowest. For example, at  $R_{12}$  two lowest minibands merge through resonant coupling, so  $\gamma_{12}$  and  $\gamma$  are exploding while  $\gamma_{23}$  changes relatively little. Thus, a peaking ratio of  $\gamma_{12}/\gamma_{23}$  makes RO decay go to nearly zero at the peak, despite homogeneous level broadening which reaches its highest extent there. Away from the peak  $\gamma$  falls off and RO persistence decreases, because of a quick drop in  $\gamma_{12}$  (Fig. 3). This is a somewhat counterintuitive example of how a quasi-bound state with shorter lifetime can be more coherent.

Since  $\gamma_{12}$  is closely related to the interminiband transition matrix element  $V_{12}$ , we can estimate the near-resonant behavior of the latter by invoking some dynamic equilibrium considerations. From elementary two-miniband model calculations (see Appendix A) we get

$$\frac{\gamma_{12}}{\gamma_{23}} = \frac{2P_1 - 1}{P_1(1 - P_1)} \quad (13)$$

$$(14)$$

Neglecting tunneling pathways between poorly aligned energy levels (e.g.  $E_1^0 \rightarrow E_2^1$  at  $\mathcal{R}_{12}^2$ ) and over many potential wells (in case of resonance across three minibands),  $V_{12} = \gamma_{12}$ . Assuming that  $\gamma_{23}$  changes over bias near  $\mathcal{R}_{12}$  adiabatically slowly compared to  $\gamma_{12}$ , we get  $V_{12} \propto \frac{(2P_1 - 1)}{P_1(1 - P_1)}$ ; with the fit for  $P_1(G)$  from Eq. 10, we can estimate the behavior of  $V_{12}$  as shown in Fig. 10. For the ideal case of  $P_1 = 0.5$  at the peak,  $\gamma_{12}$  goes to zero, which reflects a complete merger of the two lowest minibands. In principle, based on the data obtained for bias detuning dependencies of the key dynamical parameters, one can investigate near-resonant behavior of a system of coupled damped oscillators [33] beyond many simplifying approximations.

### C. RO damping and Quantum interference

RO damping originates from self-interference of a wavepacket that is facilitated by interference between small bits of wavefunction that a wavepacket constantly emits through intrawell and Bloch oscillations (denoted ‘ripples’). A wavepacket initially set in the ground miniband of a biased SL, starts to leak out into the second miniband, since the interference of the ‘ripples’ is constructive at the location of initially unpopulated MB2 and destructive at MB1. When most of the wavepacket has tunneled out into MB2, the tunneling direction reverses. This follows since now most of them are emitted from MB2. In the ideal case of zero RO damping, this reversion is a mirror process; in practice, tunneling rate to higher minibands cannot be neglected. This causes the amount of emitted ‘ripples’ to reduce faster in MB2; such an inequality breaks the mirror symmetry of the two transitions, the oscillation pattern smears out and

RO are damped more quickly, the larger is the imbalance in the rate of ‘ripples’ escape to the continuum. That is, inversely proportional to  $\gamma_{12}/\gamma_{23}$ . In other words, if  $\gamma_{23}$  cannot be neglected compared to  $\gamma_{12}$ , it breaks the anisotropy in system’s tunneling pathways: in addition to MB1 $\leftrightarrow$ MB2, there appear two additional pathways, MB1 $\leftrightarrow$ MB3 and MB2 $\leftrightarrow$ MB3 with tunneling rates being very different.

## IV. CONCLUSION

From the results of numerical simulations of near-resonant carrier dynamics at an isolated resonance, we have proposed a set of equations governing wavepacket behavior; the dynamical parameters near a resonance were found to exhibit extrema of various shapes. For overlapping resonances, a superposition of energy level anticrossings produces a shift in resonant bias. It also reduces the maximum period of RO and perturbs the dependence of dynamical parameters on bias. A superposition of Rabi and Zener resonances also allowed us to observe the transition between coherent and incoherent wavepacket dynamics, and to examine the mechanism of RO damping.

Persistence of Rabi oscillations near a resonance was demonstrated to be independent of homogeneous level broadening and to depend on the ratio of interminiband tunneling rates  $\gamma_{12}/\gamma_{23}$ , which can serve as a quantitative estimate to predict the RO damping rate.

We are grateful to NSERC Canada for continuing support via discovery grant RGPIN-3198. We would like to thank Dr. W. van Dijk for his help with the numerical algorithm implementation. The numerical simulations were carried out on the facilities of the Shared Hierarchical Academic Research Computing Network (SHARCNET:www.sharcnet.ca).

## APPENDIX A: DYNAMIC EQUILIBRIUM FOR TWO-MINIBAND SYSTEM

We consider an elementary system of two strongly interacting minibands coupled to continuum states. Further, let us denote the tunneling rate from MB $\nu$  to MB $\mu$  as  $\gamma_{\nu\mu}$ , from MB $\nu$  to continuum as  $\gamma_{\nu\infty}$  and the current occupancy of MB $\nu$  as  $\frac{p_\nu}{\rho} \equiv \tilde{\rho}_\nu$ . In steady tunneling mode, the miniband occupancies are in dynamic equilibrium. Neglecting direct tunneling from MB1 to the continuum, the flow of probability is balanced as follows:

$$\begin{cases} \frac{d}{dt} \vec{\rho} = \begin{pmatrix} \gamma_{12} & -\gamma_{21} - \gamma_{2\infty} \\ -\gamma_{12} & \gamma_{21} \end{pmatrix} \vec{\rho} \\ \frac{d}{dt} \frac{\tilde{\rho}_1}{\tilde{\rho}_1 + \tilde{\rho}_2} = \frac{d}{dt} \frac{\tilde{\rho}_2}{\tilde{\rho}_1 + \tilde{\rho}_2} \end{cases}$$

where

$$\vec{\rho} = \begin{pmatrix} \tilde{\rho}_1 \\ \tilde{\rho}_2 \end{pmatrix}$$

and the second equation expresses the conditions for dynamic equilibrium. A little algebra takes us to the quadratic equation

$$\kappa^2\gamma_{12} - \kappa(\gamma_{21} - \gamma_{12} + \gamma_{2\infty}) - \gamma_{21} = 0$$

with  $\kappa = \tilde{\rho}_1/\tilde{\rho}_2 > 1$ . Taking  $\tilde{\rho}_2 = 1 - \tilde{\rho}_1$  and assuming  $\gamma_{12} \approx \gamma_{21} = \gamma$  (which holds well in the vicinity of a resonance peak), in the steady-state limit  $t \rightarrow \infty$  we

arrive at

$$\alpha = \frac{2P_1 - 1}{P_1(1 - P_1)}$$

with the notation  $\alpha = \gamma_{\infty}/2\gamma$  and  $\gamma_{\infty} = \gamma_{2\infty}$ . Note that the extreme case of RZT corresponds to  $\alpha \rightarrow \infty$  with  $P_1 \rightarrow 1$  and of RO to  $\alpha \rightarrow 0$  with  $P_1 \rightarrow 0.5$ .

- 
- [1] C. Waschke, H. G. Roskos, K. Leo, H. Kurz, and K. Köhler, *Semicond. Sci. Technol.* **9**, 416 (1994).
- [2] K. Jin, M. Odnoblyudov, Y. Shimada, K. Hirakawa, and K. Chao, *Phys. Rev. B* **68**, 153315 (2003).
- [3] Y. Romanov and Y. Romanova, *Semiconductors* **39**, 147 (2005).
- [4] Y. Shimada, N. Sekine, and K. Hirakawa, *Applied Physics Letters* **84** (2004).
- [5] A. Zrenner, E. Beham, S. Stuffer, F. Findeis, M. Bichler, and G. Abstreiter, *Nature* **418**, 612 (2002).
- [6] Q. Wang, A. Muller, P. Bianucci, E. Rossi, Q. Xue, T. Takagahara, C. Piermarocchi, A. MacDonald, and C. Shih, *Phys. Rev. B* **72** (2005).
- [7] B. Breid, D. Witthaut, and H. Korsch, *New J. Phys.* **9**, 62 (2007).
- [8] A. Latgé, F. Ribeiro, A. Bruno-Alfonso, L. Oliveira, and H. Brandi, *Brazilian Journal of Physics* **36** (2006).
- [9] P. Abumov and D. W. L. Sprung, *Phys. Rev. B* **75** (2007).
- [10] J. Shah, *Ultrafast spectroscopy of semiconductors and semiconductor nanostructures* (Springer, 1999).
- [11] E. Beham, A. Zrenner, S. Stuffer, F. Findeis, M. Bichler, and G. Abstreiter, *Physica E* **16**, 59 (2003).
- [12] A. Vasanelli, R. Ferreira, and G. Bastard, *Phys. Rev. Lett.* **81** (2002).
- [13] P. Han, K. Jin, Y. Zhou, Q. Zhou, H. Lu, D. Guan, and G. Yang, *Europhysics letters* **72**, 1011 (2005).
- [14] P. Wilkinson, *Phys. Rev. E* **65** (5) (2002).
- [15] C. A. Moyer, *Am. J. Phys.* **72**, 352 (2004).
- [16] V. Akulin and V. Karlov, *Coherent Interaction* (Springer-Verlag, Berlin, 1992).
- [17] F. Capasso, D. Sivco, C. Sirtori, A. Hutchinson, and A. Cho, *Science* **264**, 553 (1994).
- [18] R. Ferreira and G. Bastard, *Reports on Progress in Physics* **60**, 345 (1997).
- [19] H. Brandi, A. Latgé, Z. Barticevic, and L. Oliveira, *Solid State Communications* **135**, 386 (2005).
- [20] J. Rotvig, A.-P. Jauho, and H. Smith, *Phys. Rev. Lett.* **74**, 1831 (1994).
- [21] M. Glück, M. Hankel, A. R. Kolovsky, and H. J. Korsch, *Journal of Optics B* **2**, 612 (2000).
- [22] R. Ferreira, G. Bastard, and P. Voisin, *Solid-State Electronics* **37**, 857 (1994).
- [23] G. Bastard, R. Ferreira, S. Chelles, and P. Voisin, *Phys. Rev. B* **50**, 4445 (1994).
- [24] J. Bleuse, G. Bastard, and P. Voisin, *Phys. Rev. Lett.* **60**, 220 (1987).
- [25] M. Glück, A. R. Kolovsky, and H. J. Korsch, *Phys. Rep.* **366**, 103 (2002).
- [26] M. Glück, A. R. Kolovsky, H. J. Korsch, and F. Zimmer, *Phys. Rev. B* **65** (2002).
- [27] F. Vasko and A. Kuznetsov, *Electronic states and Optical Transitions in Semiconductor Heterostructures* (Springer, 1999).
- [28] S. Gurvitz and M. Marinov, *Phys. Rev. A* **40** (1989).
- [29] S. Glutsch, *Phys. Rev. B* **69**, 235317 (2004).
- [30] A. Vojvodic, A. Blom, Z. Ma, Y. Shimada, K. Hirakawa, and K. Chao, *Solid State Communications* **136**, 580 (2005).
- [31] V. Konotop, P. Kevrekidis, and M. Salerno, *Phys. Rev. A* **72**, 023611 (2005).
- [32] G. Kohen, S. Gurvitz, and I. Bar-Joseph, *Phys. Rev. B* **47** (1993).
- [33] K. Leo, J. Shah, J. Gordon, T. Damen, D. Miller, C. Tu, and J. Cunningham, *Phys. Rev. B* **42** (1990).



